Dynamic Modeling of Soft-Material Actuators Combining Constant Curvature Kinematics and Floating-Base Approach

Maximilian Mehl*, Max Bartholdt* and Moritz Schappler

***Abstract*— Soft robotic manipulators are on the verge to their first real applications. In most cases they are actuated by fluidic pressure or tendons and molded of highly elastic material, which performs large deformation if put under stress. Performing tasks e.g. in inspection of narrow machines or endoscopy requires the actuator to be tactile and controllable. Due to their highly nonlinear behavior, model-based approaches are investigated to combine and utilize sensor information to estimate the system states of the manipulator. In this paper, equations of motion (EoM) for the well-known piecewise constant curvature (PCC) approach are extended by a floating base as it is often used in kinematic chains for legged robots and their contact with the ground. Base reaction forces and moments, which are easily measurable quantities, become visible in the EoM, if the six spatial degrees of freedom at the base of the manipulator are considered. Thereby, additional information on the system's states is obtained and used in the proposed identification scheme. Essentially, the floating base, a center-of-gravity approach and a state-of-the-art parametrization of the PCC kinematics are combined to derive and validate a Lagrangian dynamics model. On a best-case set of validation step responses, the identified inverse dynamics model performs with an accuracy of 5% to 7.6% of max. actuation torque.**

I. INTRODUCTION

In the recent decade, the intrinsic safety in human-machine-interaction of soft-material robots (SMR) and their dexterity in manipulation have often been claimed as major potential. For applications like medicine or industrial machine inspection, process time is one major influence for practicability. When it comes to dexterous and quick motion of soft-material continuum robots, a key challenge is the control of the system in a dynamic state.

Different modeling approaches have been applied in soft robotic manipulation and control. More complex models are discrete Cosserat-rod models [1], [2] or finite element models of the three-dimensional continuum like the soft robotics extension of the SOFA framework [3] as well as spline-based approaches [4]. In [5], Cosserat rod theory is applied in a rigid-flexible multi-body model describing tentacles of a swimming bio-inspired soft robot in simulation. A generalizing framework based on Lie groups and their algebra has been proposed that is capable of deriving equation of motions for flexible-rigid multi-body systems with a floating base [6]. These models mimic the general dynamic behavior of soft robotic systems, enabling controller design and research on control concepts. However, most models capable of describing slender, flexible structure with high precision are computationally expensive and thereby difficult to apply in feedback control.

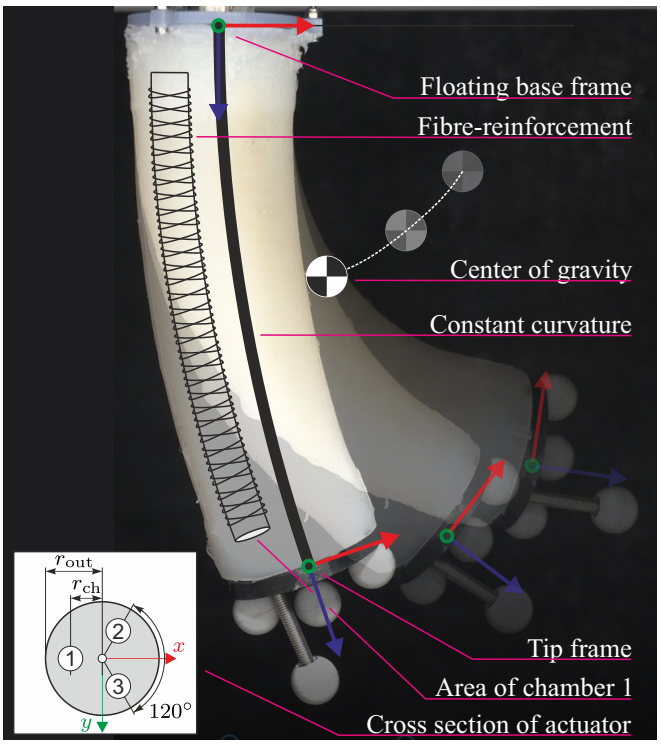

Fig. 1. Visualization of the actuator and approaches combined within this paper. The outer radius $r_{\text{out}} = 50\,\text{mm}$ and inner radius are illustrated for the reader's understanding of conducted experiments.

Due to these circumstances, the kinematic assumption of a piecewise constant curvature has been a popular approach to derive rigid-body dynamics models, which are easily implemented in feedback control. It has been shown that in combination with a feedback controller design, these models increase the accuracy in free motion [7]. A well-known disadvantage of the classic parameterization of PCC kinematics is the singularity in the straight configuration of the actuator. Recent advances made in [8] solve this problem and leverage the potential of this modeling approach.

For control, robust information on the system's state is critical. Gathering this information is a task of increasing reliable sensing capability and pairing it with accurate and efficient system models. The best model can hardly compensate poor sensor information.

For instance, in [9], [10] skin-like soft sensors are utilized

*Both authors contributed equally to this publication.

All authors are with the Leibniz University of Hannover, Institute of Mechatronic Systems, 30823 Germany. Contact: max.bartholdt@imes.uni-hannover.de

Funded by the Deutsche Forschungsgemeinschaft (DFG, German Research Foundation) under grant no. 405032969.

to increase information on the robots state. Since soft sensors capable of large deformation are still subject to on-going research, their characteristics are hardly modeled, but can be combined with data-based algorithms like long-short-term memory networks or deep-learning methods. These data-based approaches generalizes their characteristics well, but no analytical studies for e.g. sensor placement are possible and a slow response time of the sensor prevent its direct use in highly dynamic applications [10].

To overcome these limits, more conventional sensors may be applied and combined with models. Inertial measurement units (IMU) have been used and paired with pressure sensing to estimate system states by application of constant-curvature dynamics and models of pneumatic components [11]. In [12], a sophisticated design of bending actuators, enabling direct measurement of curvature combined with an improved state representation of the piecewise constant curvature kinematics with an augmented serial-link model from [13] are presented. It is also used to estimate the actuator's tip contact state, but still shows high deviations in quantity of the estimated load.

Less focus has been put on force-torque sensors. Some models capable of using their information by deriving the equation of motion with a floating base exist [6], [14], [15], [16], but neither of these works apply a dynamics model in combination with force-torque sensing at the robot's base.

In classical rigid robotics, well-identified dynamics models are key to model-based active compliance control [17]. Identification schemes using ground reaction forces like [18] have not been pursued further, presumably due to the high load on force/torque sensors mounted below the base. For soft robots however, this presents a promising approach regarding their much lower mass.

This publication contributes to recent advances on SMR modeling by deriving the equation of motion (EoM) of a soft pneumatic actuator (SPA) with a floating base using improved state parameters of [7]. Thereby, forces and moments at the actuator's base become visible in the EoM, which is an easily measurable physical quantity. The additional information is used to identify parameters within the physical model and to validate the effectiveness of the center of gravity (CoG) approach. To summarize, the contributions of this paper are

- a concept to include additional and robust information for control application,
- the derivation of the equation of motion with constant-curvature assumption and floating-base approach,
- an identification routine for system parameters based on experimental data using the systems regressor form.

The remainder of this paper is structured as follows. First, the kinematics of the soft robotic manipulator are revised, following the ideas in [8] and extending them by the floating base. Thereafter, in Sec. III the center of gravity (CoG) approach introduced in [19] is combined with nonlinear constitutive equations for elasticity and linear damping to form the EoM. To simulate the physical system, a hybrid model, which outputs are the acceleration of constant curvature states and forces as well as moments of the base, is required, as described in Sec. III-D. The experimental setup is briefly explained in Sec. IV. The adaptable identification scheme is explained in details, and validated with collected data of highly dynamic step responses of the actuator in Sec. V to Sec. 4.

II. Kinematics

The kinematics of the SPA are described by coordinate frames i using homogeneous transformation matrices

$$ {}^{i}\boldsymbol{T}_{i+1} = \begin{bmatrix} {}^{i}\boldsymbol{R}_{i+1} & \boldsymbol{t}_{i+1} \\ \boldsymbol{0} & 1 \end{bmatrix} \in \mathrm{SE}(3). \tag{1} $$

To build these matrices, parameters for configuration description are needed.

A. (Piecewise) Constant-Curvature Kinematics (PCC)

PCC-kinematics uses the assumption that the SPA bends in a way that can be described by n segments of circular arcs. Each arc can be described by a set of three parameters. There exists several possibilities of parametrization. In this paper the parametrization from [8] is used. The arc is described by three length differences. Two of them, $\Delta_{x,i}$ and $\Delta_{y,i}$, describe the length of arcs attached to the x- and y-axis of frame i and $i+1$. $\Delta_{x,i}$ describes the length difference of two arcs attached on the positive and negative x-axis in a distance d_i from the coordinate origin in frame i and $i+1$. The parameter d_i can be chosen arbitrarily, but it changes the sensitivity of the kinematics. $\Delta_{y,i}$ is described analogously using the y-axis. The third length difference δL_i describes the change in length of the center line of the segment compared to the length $L_{0,i}$ of the non-actuated segment. In this way, $\Delta_{x,i}$ and $\Delta_{y,i}$ describe the bending of the segment, while δL_i describes the elongation. These parameters are used building the rotation matrix

$$ {}^{i}\boldsymbol{R}_{i+1} = \begin{bmatrix} 1+\frac{\Delta_{x,i}^2}{\Delta_i^2}(\mathrm{c}_\Delta-1) & \frac{\Delta_{x,i}\Delta_{y,i}}{\Delta_i^2}(\mathrm{c}_\Delta-1) & \frac{\Delta_{x,i}}{\Delta_i}\mathrm{s}_\Delta \\ \frac{\Delta_{x,i}\Delta_{y,i}}{\Delta_i^2}(\mathrm{c}_\Delta-1) & 1+\frac{\Delta_{y,i}^2}{\Delta_i^2}(\mathrm{c}_\Delta-1) & \frac{\Delta_{y,i}}{\Delta_i}\mathrm{s}_\Delta \\ \frac{-\Delta_{x,i}}{\Delta_i}\mathrm{s}_\Delta & \frac{-\Delta_{y,i}}{\Delta_i}\mathrm{s}_\Delta & \mathrm{c}_\Delta \end{bmatrix} \tag{2} $$

and the translation vector

$$ \boldsymbol{t}_{i+1} = \frac{d_i(L_{0,i}+\delta L_i)}{\Delta_i^2} \begin{bmatrix} \Delta_{x,i}(1-\mathrm{c}_\Delta) \\ \Delta_{y,i}(1-\mathrm{c}_\Delta) \\ \Delta_i \mathrm{s}_\Delta \end{bmatrix} \tag{3} $$

for one constant-curvature segment. The abbreviations

$$ \Delta_i = \sqrt{\Delta_{x,i}^2 + \Delta_{y,i}^2}, \tag{4} $$

$$ \mathrm{s}_\Delta = \sin\left(\frac{\Delta_i}{d_i}\right) \quad \text{and} \quad \mathrm{c}_\Delta = \cos\left(\frac{\Delta_i}{d_i}\right) \tag{5} $$

are used.

B. Floating-Base Kinematics

For modeling, the SPA is regarded as freely moving in space. Therefore the robot's base is attached by a virtual six-DoF joint to the environment represented by a world frame. The rotation is expressed by three intrinsic elementary rotations using Cardan angles α, β and γ. The resulting rotation matrix yields

$$ {}^{0}\boldsymbol{R}_1 = \boldsymbol{R}_x(\alpha)\boldsymbol{R}_y(\beta)\boldsymbol{R}_z(\gamma). \tag{6} $$

The SPA's base translation relative to the inertial frame is described by

$$ \boldsymbol{t}_1 = \begin{bmatrix} x_0 & y_0 & z_0 \end{bmatrix}^{\mathrm{T}}. \tag{7} $$

Putting the constant-curvature- and floating-base kinematics together yields a set of $6{+}3n$ parameters $\boldsymbol{q} = [\boldsymbol{q}_0^{\mathrm{T}}, \ldots, \boldsymbol{q}_n^{\mathrm{T}}]^{\mathrm{T}}$ describing the system. The parameters consist of six-element $\boldsymbol{q}_0 = [\boldsymbol{t}_1^{\mathrm{T}}, \alpha, \beta, \gamma]^{\mathrm{T}}$ describing the floating base and $3n$-elements $\boldsymbol{q}_1, \ldots, \boldsymbol{q}_n$ describing the SPA configuration.

III. Dynamics

For parameter identification, a description of the dynamic behavior of the system is needed. To build a dynamics model, the constant-curvature segments of the SPA are treated as point masses. For minimizing the error induced by this assumption, the point mass is located at the center of gravity of the segment [19], [13]. The behavior of the hyper-elastic material is modeled by introducing a material model consisting of a nonlinear spring and a linear damping element.

A. Center of Gravity

To get the location of the center of gravity of the ith segment in frame i, ${}_{(i)}\boldsymbol{r}_{\mathrm{CoG},i}$, an integration over all points of the center line with material coordinate ξ is performed, so that

$$ {}_{(i)}\boldsymbol{r}_{\mathrm{CoG},i} = \int_0^1 {}_{(i)}\boldsymbol{p}_i(\xi, \boldsymbol{q}) \mathrm{d}\xi, \tag{8} $$

with the vector from coordinate origin of frame i to a point along the center line

$$ {}_{(i)}\boldsymbol{p}_i(\xi, \boldsymbol{q}) = \frac{d_i(L_{0,i} + \delta L_i)}{\Delta_i^2} \begin{bmatrix} \Delta_{x,i}\left(1 - \cos\left(\xi \frac{\Delta_i}{d_i}\right)\right) \\ \Delta_{y,i}\left(1 - \cos\left(\xi \frac{\Delta_i}{d_i}\right)\right) \\ \Delta_i \sin\left(\xi \frac{\Delta_i}{d_i}\right) \end{bmatrix}. \tag{9} $$

The preceding subscript (i) denotes the reference coordinate frame of a quantity, if necessary.

B. Equation of Motion

To derive the rigid-body part of the EoM, the kinetic energy E_{kin} and the potential energy E_{pot} of the CC segments' point masses are given as

$$ E_{\mathrm{kin}} = \frac{1}{2} \sum_{i=1}^{n} m_i \, {}_{(0)}\dot{\boldsymbol{r}}_{\mathrm{CoG},i}^{\mathrm{T}} \, {}_{(0)}\dot{\boldsymbol{r}}_{\mathrm{CoG},i} \tag{10} $$

$$ E_{\mathrm{pot}} = -\sum_{i=1}^{n} m_i \, {}_{(0)}\boldsymbol{g}^{\mathrm{T}} \, {}_{(0)}\boldsymbol{r}_{\mathrm{CoG},i} \tag{11} $$

using m_i as the mass of segment i and the gravitational acceleration vector ${}_{(0)}\boldsymbol{g}$. The base link's mass m_0 is neglected since only a ground-reaction force model is derived and the base does not actually move. Using the Lagrangian equations of the second kind, the mass matrix $\boldsymbol{M}(\boldsymbol{q})$, the vector of Coriolis forces $\boldsymbol{c}(\boldsymbol{q}, \dot{\boldsymbol{q}})$ and the vector of gravitational forces $\boldsymbol{g}(\boldsymbol{q})$ are derived using the computer algebra system MAPLE. To introduce the material model, a vector for spring forces and a vector for damping forces are introduced. The vector

$$ \boldsymbol{k}_i(\boldsymbol{q}_i) = \begin{bmatrix} k_{\theta_{i,3}} \Delta_{x,i}^3 + k_{\theta_{i,1}} \Delta_{x,i} \\ k_{\theta_{i,3}} \Delta_{y,i}^3 + k_{\theta_{i,1}} \Delta_{y,i} \\ k_{\delta L_{i,3}} \delta L_i^3 + k_{\delta L_{i,1}} \delta L_i \end{bmatrix} \tag{12} $$

for spring forces of one segment consists of a cubic part and a linear part, using the stiffness constants for bending $(k_{\theta_{i,3}}, k_{\theta_{i,1}})$ and elongation $(k_{\delta L_{i,3}}, k_{\delta L_{i,1}})$. The full vector

$$ \boldsymbol{k}(\boldsymbol{q}) = \begin{bmatrix} \boldsymbol{0} & \boldsymbol{k}_1^{\mathrm{T}} & \ldots & \boldsymbol{k}_n^{\mathrm{T}} \end{bmatrix}^{\mathrm{T}} \tag{13} $$

is formed by putting together $\boldsymbol{k}_1(\boldsymbol{q}_1)$ to $\boldsymbol{k}_n(\boldsymbol{q}_n)$, with the first six entries of $\boldsymbol{k}(\boldsymbol{q})$ being 0 due to the floating base. In contrast to the spring-forces vector of one segment, the damping-forces vector of one segment

$$ \boldsymbol{d}_i(\dot{\boldsymbol{q}}_i) = \begin{bmatrix} d_{\theta_i} \dot{\Delta}_{x,i} & d_{\theta_i} \dot{\Delta}_{y,i} & d_{\delta L_i} \dot{\delta L_i} \end{bmatrix}^{\mathrm{T}} \tag{14} $$

consists of only linear parts, using the damping coefficients for bending d_{θ_i} and elongation $d_{\delta L_i}$. The damping force vector $\boldsymbol{d}(\dot{\boldsymbol{q}})$ is put together in a similar way to the spring forces vector:

$$ \boldsymbol{d}(\dot{\boldsymbol{q}}) = \begin{bmatrix} \boldsymbol{0} & \boldsymbol{d}_1^{\mathrm{T}} & \ldots & \boldsymbol{d}_n^{\mathrm{T}} \end{bmatrix}^{\mathrm{T}}. \tag{15} $$

Collecting the rigid-body part and the material model, the EoM for the case of a floating base is formed as

$$ \boldsymbol{M}(\boldsymbol{q})\,\ddot{\boldsymbol{q}} + \boldsymbol{c}(\boldsymbol{q}, \dot{\boldsymbol{q}}) + \boldsymbol{g}(\boldsymbol{q}) + \boldsymbol{d}(\dot{\boldsymbol{q}}) + \boldsymbol{k}(\boldsymbol{q}) = \boldsymbol{\tau}. \tag{16} $$

The vector of generalized driving forces

$$ \boldsymbol{\tau} = \boldsymbol{\tau}_{\mathrm{base}} + \boldsymbol{\tau}_{\mathrm{CC},1} + \ldots + \boldsymbol{\tau}_{\mathrm{CC},n} \tag{17} $$

consists of different parts, where $\boldsymbol{\tau}_{\mathrm{base}}$ are the driving forces for the floating-base parameters with the last $3n$ entries being 0 and $\boldsymbol{\tau}_{\mathrm{CC},i}$ the driving forces resulting from pneumatic actuation of the segments. The base part of the model corresponds to the ground-reaction force model of [18] for rigid robots, which was derived in [18] using Lagrangian equations of the first kind with ground reaction forces as Lagrange multipliers. By setting the base motion to zero, as in [18], both approaches are equal and the Euler-angle transformation for $\boldsymbol{\tau}_{\mathrm{base}}$ does not have to be regarded.

C. Actuation

The SPA is actuated pneumatically through pressure in three chambers inside the robot, see Fig. 1 and [20]. The pressure dynamics in a chamber is modeled by a discrete

first-order lag element (PT_1), with time constant T_{PT_1}. Through the pressure in the chambers, a wrench

$$ {}_{(i)}\boldsymbol{\mathcal{F}} = \begin{bmatrix} 0 & 0 & {}_{(i)}f_z & {}_{(i)}m_x & {}_{(i)}m_y & 0 \end{bmatrix}^{\mathrm{T}} \tag{18} $$

at the tip and the base of a segment is generated, noted as

$$ {}_{(i+1)}\boldsymbol{\mathcal{F}}_{i,\mathrm{tip}} = -{}_{(i)}\boldsymbol{\mathcal{F}}_{i,\mathrm{base}} \tag{19} $$

$$ \text{with} \quad {}_{(i+1)}\boldsymbol{\mathcal{F}}_{i,\mathrm{tip}} = \begin{bmatrix} {}^{i+1}\boldsymbol{R}_i & \boldsymbol{0} \\ \boldsymbol{0} & {}^{i+1}\boldsymbol{R}_i \end{bmatrix} \boldsymbol{\mathcal{F}}_{i,\mathrm{tip}}. \tag{20} $$

The entries ${}_{(i)}f_z, {}_{(i)}m_x, {}_{(i)}m_y$ are the force/moments in frame i. The wrenches ${}_{(i+1)}\boldsymbol{\mathcal{F}}_{i,\mathrm{tip}}$ (wrench at the segments tip expressed in frame $(i+1)$ at the tip of the segment) and ${}_{(i)}\boldsymbol{\mathcal{F}}_{i,\mathrm{base}}$ (wrench at segments base expressed in frame (i) at the base of the segment) are of the same magnitude but opposite direction. The computation of the force/moments from the input pressure p_i from the chambers is performed by the relation

$$ \begin{bmatrix} f_z \\ m_x \\ m_y \end{bmatrix} = \begin{bmatrix} A & A & A \\ A\, r_{1_y} & A\, r_{2_y} & A\, r_{3_y} \\ A\, r_{1_x} & A\, r_{2_x} & A\, r_{3_x} \end{bmatrix} \begin{bmatrix} p_1 \\ p_2 \\ p_3 \end{bmatrix}. \tag{21} $$

Here the positions of the pressure chambers in the tip frame $\boldsymbol{r}_1, \boldsymbol{r}_2, \boldsymbol{r}_3$ are inserted as

$$ \boldsymbol{r}_1 = \begin{bmatrix} -r_{\mathrm{ch}} - x_{\mathrm{m}} & -y_{\mathrm{m}} \end{bmatrix}^{\mathrm{T}} \tag{22} $$

$$ \boldsymbol{r}_2 = \begin{bmatrix} r_{\mathrm{ch}} \cos(\pi + \phi) - x_{\mathrm{m}} & r_{\mathrm{ch}} \sin(\pi + \phi) - y_{\mathrm{m}} \end{bmatrix}^{\mathrm{T}} \tag{23} $$

$$ \boldsymbol{r}_3 = \begin{bmatrix} r_{\mathrm{ch}} \cos(\pi + 2\phi) - x_{\mathrm{m}} & r_{\mathrm{ch}} \sin(\pi + 2\phi) - y_{\mathrm{m}} \end{bmatrix}^{\mathrm{T}} \tag{24} $$

with the geometrical properties of the distance from the pressure chambers to the original center point r_{ch} and the angle between two chambers ϕ. Due to geometrical uncertainties, a movement of the center point is considered, with the coordinates $x_{\mathrm{m}}, y_{\mathrm{m}}$ [21]. The wrench is mapped to the driving force by the matrix relation

$$ \boldsymbol{\tau}_{\mathrm{CC},i} = \boldsymbol{A}_i \; {}_{(i+1)}\boldsymbol{\mathcal{F}}_i, \quad \text{with} \tag{25} $$

$$ \begin{aligned} \boldsymbol{A}_i = & \boldsymbol{J}_{\mathrm{g},i+1}^{\mathrm{T}}(\boldsymbol{q}) \begin{bmatrix} {}^0\boldsymbol{R}_{i+1} & \boldsymbol{0} \\ \boldsymbol{0} & {}^0\boldsymbol{R}_{i+1} \end{bmatrix} \\ & - \boldsymbol{J}_{\mathrm{g},i}^{\mathrm{T}}(\boldsymbol{q}) \begin{bmatrix} {}^0\boldsymbol{R}_i & \boldsymbol{0} \\ \boldsymbol{0} & {}^0\boldsymbol{R}_i \end{bmatrix}. \end{aligned} \tag{26} $$

The geometric Jacobian $\boldsymbol{J}_{\mathrm{g},i}$ from the origin of the inertial frame to the origin of frame i is used.

D. Hybrid Dynamics

For the purpose of deriving the model, the robot's base is regarded as moving freely in space, while the considered real system has a base at a fixed point. Therefore, the base is kept at its place by the unknown base reaction forces ($\boldsymbol{\tau}_0$), while the position, velocity and acceleration of the base are known. The boundary conditions for the robot are complimentary. The configuration is unknown, while the driving forces ($\boldsymbol{\tau}_{\mathrm{C}}$) are known (through actuation). Because of these boundary conditions, for simulation tasks hybrid-dynamics are used. That means, at certain DoFs forward, at the others inverse dynamic simulations are performed. The following deduction is based on the inverse dynamics equation (16) and the reference [22]. To form an equation for simulation, the matrix product of mass matrix and acceleration is written as

$$ \boldsymbol{M}\, \ddot{\boldsymbol{q}} = \begin{bmatrix} \boldsymbol{M}_{0,0}\, \ddot{\boldsymbol{q}}_0 + \boldsymbol{M}_{0,\mathrm{C}}\, \ddot{\boldsymbol{q}}_{\mathrm{C}} \\ \boldsymbol{M}_{\mathrm{C},0}\, \ddot{\boldsymbol{q}}_0 + \boldsymbol{M}_{\mathrm{C},\mathrm{C}}\, \ddot{\boldsymbol{q}}_{\mathrm{C}} \end{bmatrix}. \tag{27} $$

By this, the mass matrix is separated into parts corresponding either to acceleration of base or robot. Here, index 0 refers to base DoFs and index C refers to the DoFs of the constant-curvature segment. Then the EoM is sorted into known and unknown quantities, leaving an equation that can be evaluated by a numeric integration:

$$ \begin{aligned} \begin{bmatrix} \boldsymbol{\tau}_0 \\ \ddot{\boldsymbol{q}}_{\mathrm{C}} \end{bmatrix} = & \begin{bmatrix} -\boldsymbol{1} & \boldsymbol{M}_{0,\mathrm{C}} \\ \boldsymbol{0} & \boldsymbol{M}_{\mathrm{C},\mathrm{C}} \end{bmatrix}^{-1} \\ & \left(\begin{bmatrix} \boldsymbol{M}_{0,0} & \boldsymbol{0} \\ \boldsymbol{M}_{\mathrm{C},0} & \boldsymbol{1} \end{bmatrix} \begin{bmatrix} \ddot{\boldsymbol{q}}_0 \\ \boldsymbol{\tau}_{\mathrm{C}} \end{bmatrix} - \boldsymbol{c} - \boldsymbol{g} - \boldsymbol{k} - \boldsymbol{d} \right). \end{aligned} \tag{28} $$

By the boundary conditions, $\ddot{\boldsymbol{q}}_0$ is given as $\boldsymbol{0}$, which leads to $\boldsymbol{M}_{0,0}$ having no effect and has therefore not to be calculated.

IV. Experimental Setup

To deploy the introduced optimization scheme, experimental data is required. The fiber-reinforced soft pneumatic actuator (SPA) depicted in Fig. 1 possesses three individually controllable air chambers. In this setup, the three respective proportional valves are operated to switch between two states. Either they are fully opened to the environment, or to the source pressure of approx. $75\,\mathrm{kPa}$ relative pressure. This excites highly dynamic responses of the SPA, which are shown in the attached video content of this contribution. The single pneumatic chambers as well as the full SPA are operated in an open control loop, without feedback of pressure or external sensors. The experiments can therefore be performed without prior controller tuning and present a first step for identifying the robot's characteristics, which can then be used for model-based controller design and parameterization. Physical quantities measured during the experiment are the segment's tip position in space (camera system, Prime 17W, OptiTrack), pressure (142BC30A-PCB, First Sensors) in the pneumatic lines right before the actuator's air chambers as well as the base reaction forces and moments (six-axis force-torque-sensor, Nano17, ATI Industrial Automation). Except for position data, which is acquired asynchronously, all signals are recorded at $1\,\mathrm{kHz}$ at real-time. More details on software and hardware of the test bench may be found in [20].

As velocities and accelerations are required, a zero-phase moving average filter is applied to process recorded signals of the end effector position. Thereby, smooth data is acquired, which may then be differentiated numerically without amplification of large noise. The same filter is again applied to the newly gained velocity time series, to once again differentiate numerically. Thereafter, differential kinematics are used to map Cartesian data to curvilinear position, velocity and

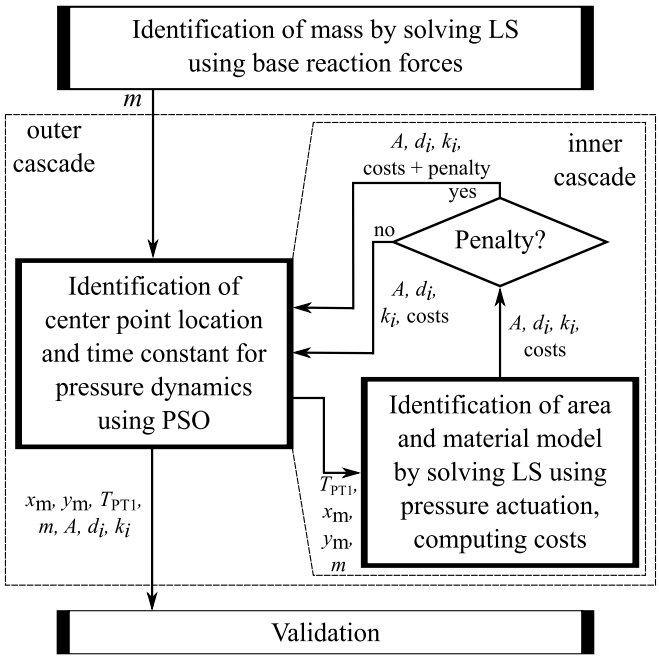

Fig. 2. Steps performed for identification.

acceleration. Any data close to straight configuration is excluded from the optimization, described next.

V. Parameter Identification

The parameter for reference length L_0, the kinematic parameter d and the distance from centerline to chamber center point are defined from CAD data beforehand. The kinematic parameter d is set to the outer radius of the SPA, which is also defined from CAD data.

For future control tasks, the remaining unknown parameters present in the model have to be estimated from measurements. For the identification in this paper, a model consisting of one constant-curvature segment with linear bending stiffness and cubic elongation stiffness is considered. The parameters chosen for identification are:

- The geometric parameters chamber area A and coordinates of the corrected center point of levers $x_\mathrm{m}, y_\mathrm{m}$ to compensate manufacturing tolerances.
- The time constant of the PT_1, T_{PT_1}.
- The dynamic parameters mass m, damping and stiffness coefficients for bending d_θ, k_θ and elongation $d_{\delta L}, k_{\delta L_1}, k_{\delta L_3}$.

Two optimization techniques are used. For the parameters linearly present in the model $(A, m, d_\theta, k_\theta, d_{\delta L}, k_{\delta L_1}, k_{\delta L_3})$ the least-squares problem (LS) considering the driving forces coming from the model evaluation ($\boldsymbol{\tau}_\mathrm{model}$) and the measured driving forces ($\boldsymbol{\tau}_\mathrm{measured}$) with error

$$e = \|\boldsymbol{\tau}_\mathrm{model} - \boldsymbol{\tau}_\mathrm{measured}\|_2^2 \tag{29}$$

has to be solved. For this the EoM (16) is rearranged into

$$\boldsymbol{\tau}_\mathrm{model} = \boldsymbol{\Psi}(\boldsymbol{q}, \dot{\boldsymbol{q}}, \ddot{\boldsymbol{q}})\,\boldsymbol{\beta}. \tag{30}$$

TABLE I
Identified parameters.

$x_\mathrm{m}/\,\mathrm{mm}$	$y_\mathrm{m}/\,\mathrm{mm}$	$T_{\mathrm{PT}_1}/\,\mathrm{ms}$	$A/\,\mathrm{mm}^2$	$m/\,\mathrm{kg}$
-0.4	-1.5	7	31	0.1806
$d_\theta/\,\frac{\mathrm{kg}}{\mathrm{s}}$	$d_{\delta L}/\,\frac{\mathrm{kg}}{\mathrm{s}}$	$k_\theta/\,\frac{\mathrm{N}}{\mathrm{m}}$	$k_{\delta L_1}/\,\frac{\mathrm{N}}{\mathrm{m}}$	$k_{\delta L_3}/\,\frac{\mathrm{N}}{\mathrm{m}^3}$
0.2301	1.8384	183.5195	251.7274	$-4.2\mathrm{e}4$

The parameters not linearly present $(x_\mathrm{m}, y_\mathrm{m}, T_{\mathrm{PT}_1})$ are identified using an overlying particle-swarm optimization (PSO). The identification process consists of three steps, which are shown in figure 2. First, the mass is estimated by (29), using the base reaction force in z-direction (f_z), setting $\tau_\mathrm{model} = f_z$ and $\beta = m$ in (30). The identified mass is given to a cascaded optimization algorithm. In the outer cascade the PSO is performed, using the result of the inner cascade as cost function. To the inner cascade the current estimation of the nonlinear parameters as well as the identified mass is handed over. With this input, (29) is solved for the remaining linear parameters, using the actuation of the constant-curvature parameters, thus setting

$$\boldsymbol{\tau}_\mathrm{model} = \begin{bmatrix}\boldsymbol{\tau}_{\Delta_x} & \boldsymbol{\tau}_{\Delta_y} & \boldsymbol{\tau}_{\delta L}\end{bmatrix}^\mathrm{T}. \tag{31}$$

The already identified mass is incorporated by multiplication of the first column of $\boldsymbol{\Psi}$ with the mass and reshaping the equation. The resulting linearly present parameters in the model are

$$\boldsymbol{\beta} = \frac{1}{A}\begin{bmatrix}1 & d_\theta & d_{\delta L} & k_\theta & k_{\delta L_1} & k_{\delta L_3}\end{bmatrix}^\mathrm{T}. \tag{32}$$

The approach of chosing combined parameters like d_θ/A is similar to the transfer from barycentric to inertial parameters in the dynamics identification of rigid-body robots [17].

The identified parameters are given back to the outer cascade, as well as the remaining error between model and measurement. The remaining error is used as the costs for the outer cascade. If a set of physically infeasible parameters is estimated (A, d_θ, k_θ, $d_{\delta L}$ or $k_{\delta L_1}$ negative) a constant penalty term, which is of a higher magnitude than the expected costs from the remaining error, is added to the costs. The PSO is performed until a minimum is reached and the estimated parameters are returned. The identified parameters consist of the physical parameters multiplied by the first parameter $1/A$. Due to the prior identification of mass, $1/A$ is identified separately as it can be seen in (32). This way identified parameters can be calculated back to physical properties. The resulting parameters are used for validating the model.

For identification and validation, the experimental results are separated into two data sets. The identification data set consisting of 30 step responses, and the validation data set consisting of 6 step responses. The identification results are shown in Table I.

VI. Validation

In the first step of validation, the error remaining on the identification data set and the validation data set is considered. The resulting mean squared error (MSE) for the

This is the author's version of an article that has been published in the IEEE RoboSoft proceedings.
Changes were made to this version by the publisher prior to publication.
The final version of record is available at https://doi.org/10.1109/RoboSoft54090.2022.9762177

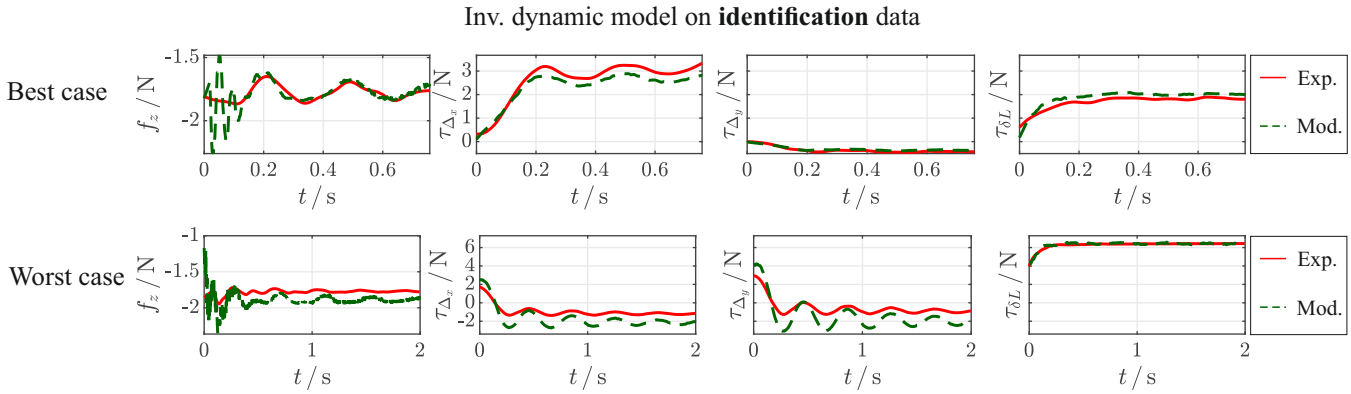

Fig. 3. Experimental results (Exp.) vs inv. dynamic model (Mod.) on the step response with best and worst average MSE.

data is computed. The results are shown in Table II. The column titled MSE shows the MSE of a DoF over the whole data set, while the columns titled MSE_{best} and $\text{MSE}_{\text{worst}}$ show the best and worst MSE achieved of a DoF at any step response in the data set.

As examples, four step responses are considered further — the steps from the identification data set with the lowest average MSE considering the SPA DoFs, and the one with the highest. The steps are shown in Fig. 3. The driving forces used for identification are shown. For mass identification, only the base reaction force in z direction is used. Regarding the worst predicted step response, a bias between model prediction and measured data is observed, while this bias is not present in the best predicted step response. The material model is estimated by the driving forces acting on the constant-curvature parameters. The best prediction is achieved, when bending around one axis is induced, although a bias in the main driving force for this step is observed. In the worst predicted step response, elongation is excited, by inserting pressure in all three chambers. The driving force for elongation, $\tau_{\delta L}$, can be predicted without a bias. The driving forces concerning bending show a bias, additionally the amplitude of the oscillations are underestimated. By actuating with pressure in all three chambers, fragments of the pressure could be visible in the measurement data of the force torque sensor, explaining the bias in f_z in the worst predicted step response. The step with the lowest average MSE from the validation data set is considered, as well as the step with the highest.

The driving forces of the best approximated step are shown in Fig. 4, the ones from the worst in Fig. 5. The base reaction forces are predicted without visible bias for both steps. The base reaction moments show a difference in amplitudes between prediction and measurements. The results of the best and worst approximated step show good agreement, hinting possibly to a good generalizing model. Base reaction moments are not considered in the identification routine, so the parameters are not optimized for predicting the base reaction moments. Also the markers for measuring the tip position are not considered in the model, which could lead to errors regarding the base reaction moments.

In the shown step, bending through actuation of τ_{Δ_x} and τ_{Δ_y} is performed. The mean of oscillation in bending direction matches in prediction the measurements, with an underestimated amplitude in τ_{Δ_y}. For elongation a bias is visible. For further validation, a hybrid dynamics simulation with the pressure input from the step response with the lowest mean MSE from the identification data set is performed. The results are shown in Fig. 6. The trajectory is shown by the evolution of the constant-curvature parameters. An overestimation of frequency in the bending parameters is visible, possibly hinting to an overestimation of stiffness parameters or underestimation of mass.

TABLE II
MSE IN BASE REACTION FORCES/MOMENTS AND DRIVING FORCES

DoF	MSE	MSE_{best}	$\text{MSE}_{\text{worst}}$
Identification data			
f_z / N^2	0.1506	0.0028	1.1834
τ_{Δ_x} / N^2	0.2466	0.0141	0.8754
τ_{Δ_y} / N^2	0.3980	0.0030	1.3076
$\tau_{\delta L}$ / N^2	0.0739	0.0046	0.2683
Validation data			
f_x / N^2	0.0130	0.0036	0.0545
f_y / N^2	0.0107	0.0023	0.0145
f_z / N^2	0.0333	0.0064	0.0640
m_x / (Nmm)^2	284.5705	19.1702	411.1973
m_y / (Nmm)^2	167.2892	54.3337	399.5674
m_z / (Nmm)^2	29.2494	0.2950	77.0389
τ_{Δ_x} / N^2	0.1852	0.0257	0.4211
τ_{Δ_y} / N^2	0.3146	0.0495	0.9014
$\tau_{\delta L}$ / N^2	0.1707	0.0138	0.5757

VII. CONCLUSIONS

In this work the governing equations of well-established models are extended by a floating base to make base reaction forces visible. Additionally, an optimization routine to experimentally determine model parameters is introduced. The underlying experiments, shown in the supplemented video material to this publication, are highly dynamic and used to identify parameters and validate the proposed method.

This is the author's version of an article that has been published in the IEEE RoboSoft proceedings.
Changes were made to this version by the publisher prior to publication.
The final version of record is available at https://doi.org/10.1109/RoboSoft54090.2022.9762177

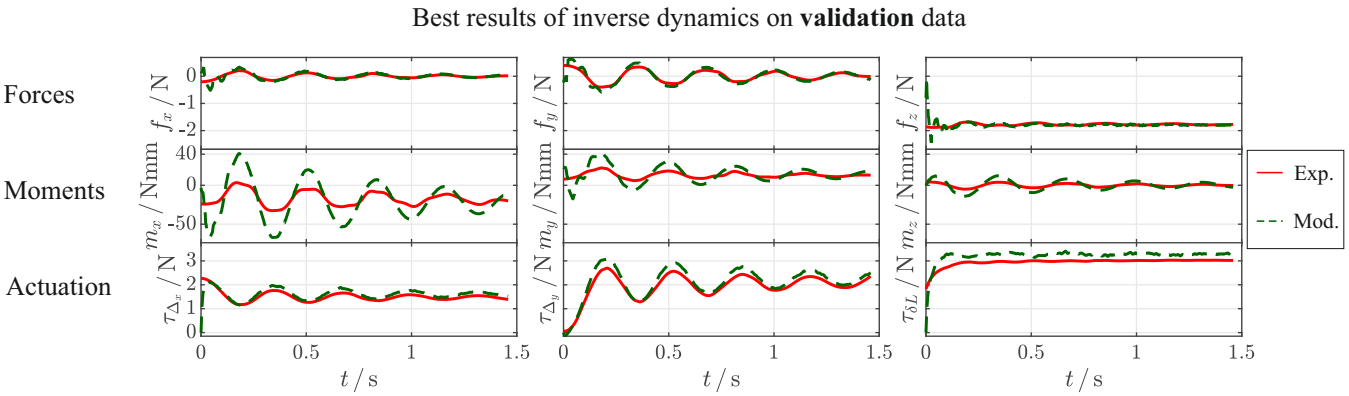

Fig. 4. Experimental results (Exp.) vs. inv. dynamic model (Mod.) for step response from validation set with best average MSE. **MSE forces in** N^2**:** 0.0055 (x), 0.0095 (y), 0.0191 (z). **MSE moments in** $(\mathrm{Nmm})^2$**:** 266.0423 (x) 54.3337 (y) 14.7790 (z). **MSE actuation in** N^2**:** 0.0378 (Δx) 0.0495 (Δy) 0.0999 (δL)

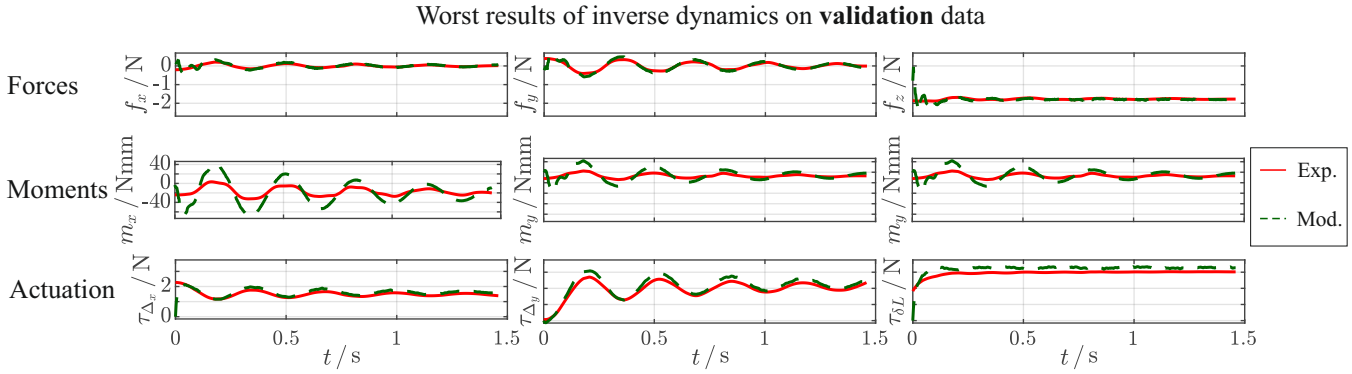

Fig. 5. Experimental results (Exp.) vs. inv. dynamic model (Mod.) for step response from validation set with worst average MSE. **MSE forces in** N^2**:** 0.0545 (x), 0.0023 (y), 0.0064 (z). **MSE moments in** $(\mathrm{Nmm})^2$**:** 19.1702 (x) 399.5674 (y) 56.6032 (z). **MSE actuation in** N^2**:** 0.4144 (Δx) 0.9014 (Δy) 0.0417 (δL)

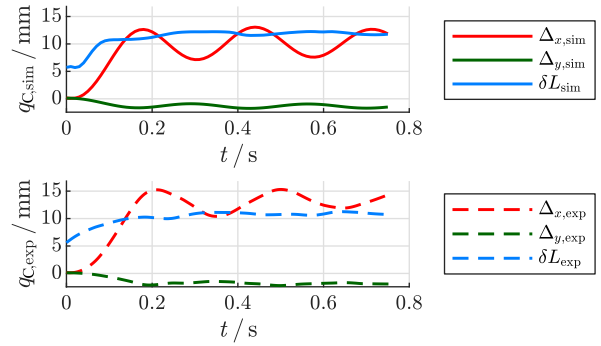

Fig. 6. Experimental (Exp.) vs. hybrid dynamics simulation (Sim.). This shows, that the model simulates the general dynamic behavior of the actuator. MSE in mm^2: 9.72 (Δ_x), 0.28 (Δ_y), 1.33 (δL)

A tuple of physically plausible values is found for kinematic parameters to account for asymmetry, caused by manufacturing uncertainties. Mass is a priori identified with measurements from the base reaction force. Thereby, the parameters successfully found by using the linear regression model of the dynamics are still interpretable, as explained in Sec. V. The approach may be extended e.g. contain more parameters within the outer optimization cascade.

The results in validation show good accordance of the inverse dynamics model and experiments in actuation space regarding the MSE of $0.0378\,\mathrm{N}^2$ to $0.0999\,\mathrm{N}^2$. This equals 5% to 7.64% of the maximum measured value. Measured moments at the base deviate from the calculated ones for all DoF and thus show limitations of our approach. Further investigation will consider refinement of the model and its application in multiple control scenarios.

References

[1] S. H. Sadati, S. E. Naghibi, A. Shiva, B. Michael, L. Renson, M. Howard, C. D. Rucker, K. Althoefer, T. Nanayakkara, S. Zschaler, C. Bergeles, H. Hauser, and I. D. Walker, "TMTDyn: A Matlab package for modeling and control of hybrid rigid–continuum robots based on discretized lumped systems and reduced-order models," *The International Journal of Robotics Research*, vol. 40, no. 1, pp. 296–347, 2020.

[2] F. Campisano, S. Caló, A. A. Remirez, J. H. Chandler, K. L. Obstein, R. J. Webster, and P. Valdastri, "Closed-loop control of soft continuum manipulators under tip follower actuation," *The International Journal of Robotics Research*, vol. 40, no. 6-7, pp. 923–938, 2021.

[3] O. Goury, B. Carrez, and C. Duriez, "Real-time simulation for control of soft robots with self-collisions using model order reduction for contact forces," *IEEE Robotics and Automation Letters*, vol. 6, no. 2, pp. 3752–3759, 2021.

[4] M. Wiese, K. Rustmann, and A. Raatz, "Kinematic modeling of a soft pneumatic actuator using cubic Hermite splines," in *2019 IEEE/RSJ International Conference on Intelligent Robots and Systems (IROS)*. IEEE, 2019.

[5] F. Renda, F. Giorgio-Serchi, F. Boyer, C. Laschi, J. Dias, and L. Seneviratne, "A unified multi-soft-body dynamic model for underwater soft robots," *The International Journal of Robotics Research*, vol. 37, no. 6, pp. 648–666, 2018.

[6] F. Renda and L. Seneviratne, "A geometric and unified approach for modeling soft-rigid multi-body systems with lumped and distributed degrees of freedom," in *2018 IEEE International Conference on Robotics and Automation (ICRA)*. IEEE, 2018.

[7] C. D. Santina, R. K. Katzschmann, A. Bicchi, and D. Rus, "Model-based dynamic feedback control of a planar soft robot: trajectory tracking and interaction with the environment," *The International Journal of Robotics Research*, vol. 39, no. 4, pp. 490–513, 2020.

[8] C. D. Santina, A. Bicchi, and D. Rus, "On an improved state parametrization for soft robots with piecewise constant curvature and its use in model based control," *IEEE Robotics and Automation Letters*, vol. 5, no. 2, pp. 1001–1008, 2020.

[9] R. L. Truby, C. D. Santina, and D. Rus, "Distributed proprioception of 3D configuration in soft, sensorized robots via deep learning," *IEEE Robotics and Automation Letters*, vol. 5, no. 2, pp. 3299–3306, 2020.

[10] T. G. Thuruthel, B. Shih, C. Laschi, and M. T. Tolley, "Soft robot perception using embedded soft sensors and recurrent neural networks," *Science Robotics*, vol. 4, no. 26, 2019.

[11] S. Ibrahim, J. C. Krause, A. Olbrich, and A. Raatz, "Modeling and reconstruction of state variables for low-level control of soft pneumatic actuators," *Frontiers in Robotics and AI*, vol. 8, 2021.

[12] Y. Toshimitsu, K. W. Wong, T. Buchner, and R. Katzschmann, "SoPrA: Fabrication & dynamical modeling of a scalable soft continuum robotic arm with integrated proprioceptive sensing," in *2021 IEEE/RSJ International Conference on Intelligent Robots and Systems (IROS)*. IEEE, 2021.

[13] R. K. Katzschmann, C. D. Santina, Y. Toshimitsu, A. Bicchi, and D. Rus, "Dynamic motion control of multi-segment soft robots using piecewise constant curvature matched with an augmented rigid body model," in *2019 2nd IEEE International Conference on Soft Robotics (RoboSoft)*. IEEE, 2019.

[14] I. S. Godage, T. Nanayakkara, and D. G. Caldwell, "Locomotion with continuum limbs," in *2012 IEEE/RSJ International Conference on Intelligent Robots and Systems*. IEEE, 2012.

[15] C. Yang, J. Yang, X. Wang, and B. Liang, "Control of space flexible manipulator using soft actor-critic and random network distillation," in *2019 IEEE International Conference on Robotics and Biomimetics (ROBIO)*. IEEE, 2019.

[16] H. Mochiyama and T. Suzuki, "Dynamical modelling of a hyper-flexible manipulator," in *Proceedings of the 41st SICE Annual Conference. SICE 2002.* Soc. Instrument & Control Eng. (SICE), 2002.

[17] W. Khalil and E. Dombre, *Modeling, Identification and Control of Robots*. CRC Press, 2002.

[18] B. Raucent, G. Campion, G. Bastin, J. Samin, and P. Willems, "Identification of the barycentric parameters of robot manipulators from external measurements," *Automatica*, vol. 28, no. 5, pp. 1011–1016, 1992.

[19] I. S. Godage, R. Wirz, I. D. Walker, and R. J. Webster, "Accurate and efficient dynamics for variable-length continuum arms: A center of gravity approach," *Soft Robotics*, vol. 2, no. 3, pp. 96–106, 2015.

[20] M. Bartholdt, M. Wiese, M. Schappler, S. Spindeldreier, and A. Raatz, "A parameter identification method for static Cosserat rod models: Application to soft material actuators with exteroceptive sensors," in *2021 IEEE/RSJ International Conference on Intelligent Robots and Systems (IROS)*. IEEE, 2021.

[21] S. R. Eugster, J. Harsch, M. Bartholdt, M. Herrmann, M. Wiese, and G. Capobianco, "Soft pneumatic actuator model based on a pressure-dependent spatial nonlinear rod theory," *IEEE Robotics and Automation Letters*, vol. 7, no. 2, pp. 2471–2478, 2022.

[22] R. Featherstone, *Rigid Body Dynamics Algorithms*. Springer Science & Business Media, 2008.